International Journal of Heat and Mass Transfer 127 (2018) 245–256

Contents lists available at ScienceDirect

International Journal of Heat and Mass Transfer

journal homepage: www.elsevier.com/locate/ijhmt

Heat transfer enhancement strategies in a swirl flow minichannel heat sink based on hydrodynamic receptivity

Benjamín Herrmann-Priesnitz [a,*], Williams R. Calderón-Muñoz [a,b], Gerardo Diaz [c], Rodrigo Soto [d]

[a] Department of Mechanical Engineering, FCFM, Universidad de Chile, Beauchef 851, Santiago, Chile
[b] Energy Center, FCFM, Universidad de Chile, Av. Tupper 2007, Santiago, Chile
[c] Department of Mechanical Engineering, University of California-Merced, 5200 North Lake Rd., Merced, CA 95343, USA
[d] Physics Department, FCFM, Universidad de Chile, Av. Blanco Encalada 2008, Santiago, Chile

ARTICLE INFO

Article history:
Received 1 February 2018
Received in revised form 7 June 2018
Accepted 13 July 2018
Available online 29 July 2018

Keywords:
Hydrodynamic stability
Heat transfer enhancement
Minichannel heat sink
Swirl flow

ABSTRACT

The swirl flow minichannel heat sink has shown to be a promising alternative for thermal management of high heat flux applications, such as electronics and concentrated photovoltaics. Effective heat transfer enhancement strategies for this device are identified by studying the receptivity of temperature disturbances to a momentum forcing input. Steady state laminar flow is calculated numerically and experimental measurements are carried out to validate the results for subcritical Reynolds numbers. Using the framework of nonmodal stability theory, a harmonically driven linear perturbation problem is formulated, and the methodology to apply the local and parallel flow approximations based on order of magnitude arguments is detailed. The input-output response of temperature perturbations to forcing of the radial, azimuthal, and wall-normal momentum components is calculated for a range of wavenumbers, waveangles and temporal frequencies. The largest amplification is presented by streamwise vortices and streaks, followed by axisymmetric inward travelling waves, and then by streamwise propagating waves. Micromachining the channel walls with streamwise spiral grooves is proposed as a heat transfer enhancement technique. Excitation of streamwise independent structures in the wall-normal direction is expected, therefore maximum amplification should be obtained. Due to its simple implementation, we also propose using a pulsating flow rate as a heat transfer enhancement technique. Receptivity results for streamwise propagating waves of radial forcing show a response curve with moderate amplification for a wide range of actuation frequencies. Experimental work is conducted to measure the performance of the swirl flow channel heat sink using flow pulsations at the range of forcing frequencies suggested by the receptivity study. Compared to the unforced case, a lower wall temperature (up to 5 °C cooler) was observed with pulsations, at the same imposed heat flux and flow rate. To get the same wall temperature as in the unforced case, a pumping power reduction of up to 26.6% was observed, and using the same pumping power resulted in up to a 10.3% Nusselt enhancement. Hydrodynamic receptivity was successfully used to identify effective heat transfer enhancement strategies, resulting in a significant performance improvement for the swirl flow channel heat sink. This physics based approach can be extended to other techniques, for instance, to select the wavelength of a wavy surface, the periodicity of surface roughness elements, or the frequency of acoustic vibrations.

1. Introduction

High heat flux removal is required in numerous industrial applications, such as electronics cooling [1], laser diodes cooling [2], and concentrated photovoltaics [3]. Thermal management is important for the performance, safety, and lifetime of these devices [4,5], which is why high heat flux cooling technologies is one of the most active fields of heat transfer research today. Most promising solutions using single phase liquid cooled heat sinks include designs with jet impingement, flow through porous media, and microchannels [6–8]. During the last decade, several researchers have investigated single-phase heat transfer enhancement techniques for microchannels and minichannels with the goal of extending the applicability of single-phase cooling for critical applications, before more aggressive techniques, such as flow boiling, are considered [9–13]. Typical strategies include passive techniques, such as surface roughness, flow disruptions, channel curvature, out of plane

* Corresponding author.
E-mail address: bherrman@ing.uchile.cl (B. Herrmann-Priesnitz).

https://doi.org/10.1016/j.ijheatmasstransfer.2018.07.077
0017-9310/

mixing and fluid additives, as well as active techniques, such as vibration, electrostatic fields and flow pulsation [9]. In general, most advances on heat transfer augmentation are inspired by techniques that have proven to be successful in the past.

The swirl flow channel heat sink consists of an annular cavity closed at the top and bottom, where fluid is admitted through the outer radius, it spirals radially inward and exits through the inner radius, heat is removed from one of the cavity walls whereas the other one is insulated. This device was designed and first studied by Ruiz and Carey in 2012 [14,15]. In subsequent work in 2015, they built a prototype and compared experimental measurements using water to an analytical model for the heat and momentum transport in the heat sink. They found that the model underpredicted both, the pressure drop and total heat flux, due to not taking into account secondary flows and instabilities induced by rotation. The results from Ruiz and Carey also showed that the design is promising, a heat flux of 113 W/cm^2 was achieved while maintaining a surface temperature below 80 °C and a ratio of pumping power to heat rate of 0.03% [14,15]. Steady state flow in this heat sink was studied numerically using integral methods by Herrmann-Priesnitz et al. in 2016 [16], and different boundary layer structures were observed depending on the governing parameters. In subsequent work, a thermal design exploration of this device was carried out [17]. Rotation of the fluid induces a crossflow and entrainment, which was found to enhance convective heat transfer considerably due to motion of fluid towards the heat exchange surface. This effect depends on the structure of hydrodynamic boundary layers, and is intensified for small flow inlet angles and high Reynolds number. Device performance was compared to other single phase microchannel heat sinks for high heat cooling applications reviewed by Agostini et al. [6]. Although the swirl flow channel heat sink presented about 25% of the heat flux achieved with other devices, the total pressure drop was much lower, resulting in a ratio of pumping power to heat rate that of about 20% of the lowest value reported in Ref. [6]. It was concluded that the swirl flow channel heat sink is suitable for applications where low pumping cost is required. Furthermore, for high heat flux applications, there is a significant margin to use heat transfer enhancement techniques even if the pumping cost increases.

The velocity profiles found in this type of channel are similar to those observed in other rotating boundary layer flows, such as von Kármán, Ekman and Bödewadt flows. The first experimental observation of stationary crossflow vortices and the first theoretical stability analysis for the rotating disc flow were presented by Gregory et al. [18]. Work on the modal and spatial stability continued with Malik, who computed the neutral curves for stationary disturbances using the parallel flow approximation [19]. Lingwood followed by studying the absolute or convective nature of the instabilities [20]. More recently, Serre et al. and Lopez et al. used DNS and found that the Bödewadt layer is unstable to axisymmetric circular radial waves and three-dimensional multi-armed spiral waves [21,22]. In a follow up study, Do et al. showed that in the absence of any external forcing, the circular waves are transitory, but low amplitude forcing can sustain them indefinitely [23].

Over the past two decades, nonmodal stability theory has emerged to provide a more complete picture of the linear perturbation dynamics for fluid flows using an initial-value problem formulation [24–27]. This framework allows the incorporation of an external harmonic forcing term that may represent free-stream turbulence, wall roughness, acoustic perturbations or body forces among others. The response of the system to these external disturbances, i.e. receptivity of the flow, is determined by the particular solution to the harmonically driven problem. A componentwise receptivity analysis for plane channel flows was carried out by Jovanović and Bamieh in 2005 [28]. Their results showed how the roles of Tollmien-Schlichting (T-S) waves, oblique waves, and streamwise vortices and streaks can be explained as input-output resonances of the spatio-temporal frequency responses. Therefore, one can identify efficient mechanisms to favor the emergence of specific flow structures. In a similar manner, a receptivity analysis can be used to identify efficient mechanisms to enhance convective heat transfer. This approach, based on physics rather than experience has not been presented elsewhere.

In this work, we use the framework of nonmodal stability theory to study the response of temperature disturbances to a momentum forcing. The steady state flow is calulated using the integral method developed in Ref. [16] for the velocity field, and the spatial discretization presented in [17] followed by matrix inversion is used for the temperature field. A swirl flow channel heat sink is fabricated and experimental measurements of the pressure drop and wall temperature are used to validate the base flow in the laminar range of flow rates. A harmonically driven linear perturbation problem is formulated, and the methodology to apply the local and parallel flow approximations based on order of magnitude arguments is detailed. The amplification of temperature perturbations to forcing of the radial, azimuthal, and wall-normal momentum components is calculated for a range of wavenumbers and temporal frequencies. Characteristics of the most receptive types of forcing are used to identify effective heat transfer enhancement techniques, resulting in a significant performance improvement for the swirl flow channel heat sink.

2. Theoretical analysis

2.1. Steady state flow

The swirl flow minichannel heat sink consists of an annular cavity, which is open at the outer and inner radii, r_o and r_i, respectively. The top and bottom boundaries are solid walls with a separation of $2h$, and it has a very small aspect ratio $h/r_o \ll 1$. Incompressible fluid enters the channel at r_o with an inlet angle θ_o with respect to the tangent, it spirals radially inward, and exits through r_i, heat is removed from the top channel wall whereas the bottom one is insulated. A schematic of the heat sink design is shown in Fig. 1.

The steady state flow is axisymmetric, it presents a boundary layer nature, and viscous dissipation and buoyant effects are negligible, therefore the governing steady state equations are

$$\frac{1}{r}\frac{\partial(rU)}{\partial r}+\frac{\partial W}{\partial z}=0, \tag{1a}$$

$$U\frac{\partial U}{\partial r}+W\frac{\partial U}{\partial z}-\frac{V^2}{r}=-\frac{1}{\rho}\frac{\partial P}{\partial r}+\nu\frac{\partial^2 U}{\partial z^2}, \tag{1b}$$

$$U\frac{\partial V}{\partial r}+W\frac{\partial V}{\partial z}+\frac{UV}{r}=\nu\frac{\partial^2 V}{\partial z^2}, \tag{1c}$$

$$0=-\frac{1}{\rho}\frac{\partial P}{\partial z}, \tag{1d}$$

$$U\frac{\partial T}{\partial r}+W\frac{\partial T}{\partial z}=\alpha\frac{\partial^2 T}{\partial z^2}, \tag{1e}$$

$$\begin{aligned} z=h:&\quad \mathbf{U}=0,\quad \kappa\frac{\partial T}{\partial z}=q''_w,\\ r=r_o:&\quad \mathbf{U}=U_o(1,\cot\theta_o,0)^T,\quad T=T_o,\\ z=-h:&\quad \mathbf{U}=0,\quad \frac{\partial T}{\partial z}=0,\\ r=r_i:&\quad P=0, \end{aligned} \tag{1f}$$

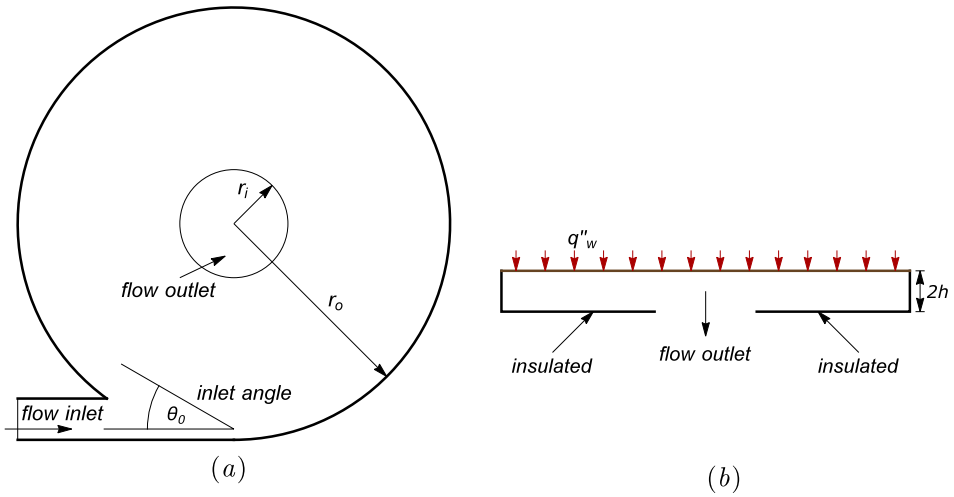

Fig. 1. Schematic of a swirl flow microchannel heat sink. (a) Top view. (b) Cross-sectional view.

where $\mathbf{U} = (U, V, W)^T$ is the velocity field in cylindrical coordinates $(\hat{\mathbf{r}}, \hat{\boldsymbol{\theta}}, \hat{\mathbf{z}})$, P is the pressure, T is the temperature, ρ is the density, ν is the kinematic viscosity, and κ and α are thermal conductivity and thermal diffusivity, respectively. Boundary conditions are shown in Eq. (1f): no-slip and a constant heat flux at the top wall, no-slip and zero heat flux at the bottom wall, specified velocity components and temperature at the inlet, and a reference pressure is set at the outlet.

The parameters governing the steady state flow are the inlet angle θ_o, the flow rate Reynolds number defined as $Re_o = U_o h^2/(\nu r_o)$, and the Prandtl number $Pr = \nu/\alpha$. Numerical solution to Eqs. (1a)–(1d) with boundary conditions (1f) is obtained using the integral method developed in Ref. [16]. Once the velocity field is known, Eq. (1e) subject to boundary conditions (1f) becomes a linear parabolic PDE problem, therefore it can be solved using spatial discretization followed by matrix inversion. Specifically, we use the Chebyshev collocation method to discretize in the z direction and a 2^{nd}-order upwind scheme to discretize in the r direction, as presented in [17].

In this work, we study the local behavior of the system around a certain radial position r. The flow can be regarded as locally Cartesian in the coordinates $(\hat{\mathbf{r}}, r\hat{\boldsymbol{\theta}}, \hat{\mathbf{z}})$ if the radius is sufficiently large compared to the half-height of the channel i.e., $\varepsilon = h/r \ll 1$. Due to the boundary layer nature of the flow, the normal velocity component W is much smaller than those parallel to the walls U and V, and radial dependence of $\mathbf{U}$ and T is much smaller than their dependence in the direction normal to wall. In fact, these are smaller by a factor of order $O(\varepsilon)$, and by neglecting them we get $\mathbf{U} \approx (U(z), V(z), 0)^T$ and $T \approx T(z)$, which is known in literature as the parallel flow approximation.

2.2. Linearized perturbation equations

Linearizing the incompressible Navier-Stokes and energy equations about the base flow $(U(z), V(z), 0)^T$ and $T(z)$ yields the following system of equations

$$\frac{\partial u}{\partial r} + \frac{1}{r}\frac{\partial v}{\partial \theta} + \frac{\partial w}{\partial z} = 0, \tag{2a}$$

$$\frac{\partial u}{\partial t} + U\frac{\partial u}{\partial r} + \frac{V}{r}\frac{\partial u}{\partial \theta} + wU' = -\frac{\partial p}{\partial r} + \frac{1}{Re}\nabla^2 u + f_u, \tag{2b}$$

$$\frac{\partial v}{\partial t} + U\frac{\partial v}{\partial r} + \frac{V}{r}\frac{\partial v}{\partial \theta} + wV' = -\frac{1}{r}\frac{\partial p}{\partial \theta} + \frac{1}{Re}\nabla^2 v + f_v, \tag{2c}$$

$$\frac{\partial w}{\partial t} + U\frac{\partial w}{\partial r} + \frac{V}{r}\frac{\partial w}{\partial \theta} = -\frac{\partial p}{\partial z} + \frac{1}{Re}\nabla^2 w + f_w, \tag{2d}$$

$$\frac{\partial \tau}{\partial t} + U\frac{\partial \tau}{\partial r} + \frac{V}{r}\frac{\partial \tau}{\partial \theta} + wT' = \frac{1}{RePr}\nabla^2 \tau + f_\tau, \tag{2e}$$

where $\mathbf{u} = (u, v, w)^T$ is the perturbation velocity, p is the perturbation pressure, τ is the perturbation temperature, and $'$ denotes differentiation of the base flow with respect to to z. Here, ∇^2 stands for $\frac{\partial^2}{\partial r^2} + \frac{1}{r^2}\frac{\partial^2}{\partial \theta^2} + \frac{\partial^2}{\partial z^2}$, which is the Cartesian Laplace operator in the local coordinates $(\hat{\mathbf{r}}, r\hat{\boldsymbol{\theta}}, \hat{\mathbf{z}})$. We have added the external forcing terms $(f_u, f_v, f_w)^T$ to the momentum equations and f_τ to the energy equation, which will later be used for the receptivity analysis. Eqs. (2) have been nondimensionalized using the half-height of the channel h as the characteristic length scale, the velocity magnitude $\sqrt{U^2 + V^2}$ at the midplane of the channel as the characteristic velocity scale, T_o is set as the temperature reference, and $T_i - T_o$ is used as the characteristic temperature difference scale, where T_i is the average temperature at the inner radius (outlet). The temporal evolution problem for the perturbations is completed with appropriate initial conditions, and the boundary conditions i.e., $u = v = w = \tau = 0$ at $z = \pm 1$. Eqs. (2) have coefficients that do not depend on r and θ, this allows for the perturbation variables to be expanded as Fourier modes in these directions $\mathbf{u}(r, \theta, z, t) = \hat{\mathbf{u}}(z, t)\, e^{i(\alpha r + m\theta)}$, where α is the radial wavenumber, and m is the integer azimuthal wavenumber. Identical expansions are carried out for the perturbation pressure, perturbation temperature, and external forcing terms. Governing equations are simplified to

$$i\alpha\hat{u} + i\beta\hat{v} + \mathcal{D}\hat{w} = 0, \tag{3a}$$

$$\frac{\partial \hat{u}}{\partial t} + i(\alpha U + \beta V)\hat{u} + U'\hat{w} = -i\alpha\hat{p} + \frac{1}{Re}\left(\mathcal{D}^2 - k^2\right)\hat{u} + \hat{f}_u, \tag{3b}$$

$$\frac{\partial \hat{v}}{\partial t} + i(\alpha U + \beta V)\hat{v} + V'\hat{w} = -i\beta\hat{p} + \frac{1}{Re}\left(\mathcal{D}^2 - k^2\right)\hat{v} + \hat{f}_v, \tag{3c}$$

$$\frac{\partial \hat{w}}{\partial t} + i(\alpha U + \beta V)\hat{w} = -\mathcal{D}\hat{p} + \frac{1}{Re}\left(\mathcal{D}^2 - k^2\right)\hat{w} + \hat{f}_w, \tag{3d}$$

$$\frac{\partial \hat{\tau}}{\partial t} + i(\alpha U + \beta V)\hat{\tau} + T'\hat{w} = \frac{1}{RePr}\left(\mathcal{D}^2 - k^2\right)\hat{\tau} + \hat{f}_\tau, \tag{3e}$$

where $\beta = m/r$, the total wavenumber is $k = (\alpha^2 + \beta^2)^{\frac{1}{2}}$, and $\mathcal{D}$ denotes differentiation with respect to z of the perturbation variables. A more compact formulation is obtained by rewriting the system in terms of the normal vorticity $\hat{\eta}$ and the normal velocity $\hat{w}$ instead of the primitive variables. To do this, we first derive the transport equation for $\hat{\eta}$ by taking the z component of the curl of the momentum Eqs. (3b)–(3d). Secondly, we obtain an expression for the pressure by taking the divergence of the momentum Eqs. (3b)–(3d) and using the continuity Eq. (3a). The resulting expression is substituted into Eq. (3d) to eliminate $\hat{p}$ from the system

$$\mathcal{M}\frac{\partial \hat{w}}{\partial t} = -\mathrm{i}\mathcal{M}(\alpha U + \beta V)\hat{w} - \mathrm{i}(\alpha U'' + \beta V'')\hat{w} - \frac{1}{Re}\mathcal{M}^2\hat{w} + \mathrm{i}\alpha\mathcal{D}\hat{f}_u + \mathrm{i}\beta\mathcal{D}\hat{f}_v + k^2\hat{f}_w, \tag{4a}$$

$$\frac{\partial \hat{\eta}}{\partial t} = -\mathrm{i}(\alpha U + \beta V)\hat{\eta} - \frac{1}{Re}\mathcal{M}\hat{\eta} + \mathrm{i}(\alpha V' - \beta U')\hat{w} + \mathrm{i}\beta\hat{f}_u - \mathrm{i}\alpha\hat{f}_v, \tag{4b}$$

$$\frac{\partial \hat{\tau}}{\partial t} = -\mathrm{i}(\alpha U + \beta V)\hat{\tau} - \frac{1}{RePr}\mathcal{M}\hat{\tau} - T'\hat{w} + \hat{f}_\tau, \tag{4c}$$

where $\mathcal{M} = \left(k^2 - \mathcal{D}^2\right)$. The boundary conditions for the normal vorticity, normal velocity, and temperature become $\mathcal{D}\hat{w}(\pm 1) = \hat{w}(\pm 1) = \hat{\eta}(\pm 1) = \hat{\tau}(\pm 1) = 0$. Eqs. (4) are discretized using the Chebyshev collocation method and the operator $\mathcal{D}$ is replaced with the Chebyshev differentiation matrix $\mathbf{D}$. We obtain a linear dynamical system where the state variables are the normal velocity, normal vorticity, and temperature evaluated at the collocation points. The matrix representation of the system is

$$\frac{\mathrm{d}}{\mathrm{d}t}\begin{bmatrix}\hat{w}\\ \hat{\eta}\\ \hat{\tau}\end{bmatrix} = \underbrace{\begin{bmatrix}\mathbf{L_{OS}} & 0 & 0\\ \mathbf{L_{C1}} & \mathbf{L_{SQ}} & 0\\ \mathbf{L_{C2}} & 0 & \mathbf{L_H}\end{bmatrix}}_{\mathbf{L}}\begin{bmatrix}\hat{w}\\ \hat{\eta}\\ \hat{\tau}\end{bmatrix} + \underbrace{\begin{bmatrix}\mathrm{i}\alpha\mathbf{M}^{-1}\mathbf{D} & \mathrm{i}\beta\mathbf{M}^{-1}\mathbf{D} & \mathbf{M}^{-1}k^2 & 0\\ \mathrm{i}\beta & -\mathrm{i}\alpha & 0 & 0\\ 0 & 0 & 0 & 1\end{bmatrix}}_{\mathbf{B}}\begin{bmatrix}\hat{f}_u\\ \hat{f}_v\\ \hat{f}_w\\ \hat{f}_\tau\end{bmatrix}, \tag{5}$$

where $\mathbf{M}$ is the discretized representation of $\mathcal{M}$, and $\mathbf{L_{OS}}, \mathbf{L_{SQ}}$, and $\mathbf{L_{C1}}$ are the familiar Orr-Sommerfeld, Squire, and coupling operators for a base flow that has velocity components along both, the spanwise and streamwise directions. The matrix denoted as $\mathbf{L_H}$ corresponds to the linearized heat equation operator, and $\mathbf{L_{C2}}$ is the coupling term with the normal velocity perturbation. The rate of change of the state vector $\hat{\mathbf{q}} = (\hat{w}, \hat{\eta}, \hat{\tau})^T$ is related to its current state by operator $\mathbf{L}$, and to the input forcing $\hat{\mathbf{f}} = (\hat{f}_u, \hat{f}_v, \hat{f}_w, \hat{f}_\tau)^T$ by operator $\mathbf{B}$. The system can be written in compact notation as follows

$$\frac{\mathrm{d}\hat{\mathbf{q}}}{\mathrm{d}t} = \mathbf{L}\hat{\mathbf{q}} + \mathbf{B}\hat{\mathbf{f}}, \tag{6a}$$

$$\hat{\mathbf{y}} = \mathbf{C}\hat{\mathbf{q}}, \tag{6b}$$

where $\hat{\mathbf{y}}$ is a an observation of the state $\hat{\mathbf{q}}$ through the linear mapping $\mathbf{C}$. Eq. (6) governs the dynamics of the perturbation variables for a generalized forcing and a linear observable function. In particular, we are interested in the response of the temperature field to an external harmonic momentum forcing in the radial, azimuthal or axial component.

2.3. Componentwise response

For an external harmonic forcing $\hat{\mathbf{f}}(t) = \tilde{\mathbf{f}}\exp(\mathrm{i}\omega t)$, the particular solution to Eqs. (6) is given by

$$\hat{\mathbf{y}} = \mathbf{C}(\mathrm{i}\omega\mathbf{I} - \mathbf{L})^{-1}\mathbf{B}\hat{\mathbf{f}}. \tag{7}$$

For an asymptotically stable flow, this solution represents the long-term response of the system. The operator $\mathcal{H}(\alpha, \beta, \omega) = \mathbf{C}(\mathrm{i}\omega\mathbf{I} - \mathbf{L})^{-1}\mathbf{B}$ is closely related to the concept of the transfer function of a linear time-invariant system, so that $\hat{\mathbf{y}} = \mathcal{H}(\alpha, \beta, \omega)\hat{\mathbf{f}}$. Hence, this operator maps the input forcing $\hat{\mathbf{f}}$ to the observable $\hat{\mathbf{y}}$, and it is a function of the forcing frequency ω and the wavenumbers α and β. We define the componentwise transfer function, $\mathcal{H}_{xs}(\alpha, \beta, \omega)$, as the mapping from the x-component of the forcing $\hat{\mathbf{f}}$ to the s-component of the observable $\hat{\mathbf{y}}$, and it is obtained by zeroing out the corresponding columns of $\mathbf{B}$ and rows of $\mathbf{C}$. In this work we are interested in the response of the disturbance temperature τ to an external forcing in each of the momentum components, i.e., we want to measure $\mathcal{H}_{u\tau}, \mathcal{H}_{v\tau}$ and $\mathcal{H}_{w\tau}$.

2.3.1. Choice of measure

An important question we still need to answer is what measure should we use to quantify the size of disturbances. In order to measure the momentum forcing (input) and the disturbance temperature (output), we need to define an energy norm $||\cdot||_E$. A physically relevant choice to measure the forcing is the kinetic energy [29], and for the output we use the standard (Euclidean) L_2-norm, as it measures the deviation of the disturbance temperature field from the steady state temperature field. Hence, for a state vector $\hat{\mathbf{q}} = (\hat{u}, \hat{v}, \hat{w}, \hat{\tau})^T$, the following energy norm is defined

$$||\hat{\mathbf{q}}||_E^2 = \int_{-1}^{1}\left[\frac{1}{2}\left(|\hat{u}|^2 + |\hat{v}|^2 + |\hat{w}|^2\right) + |\hat{\tau}|^2\right]\mathrm{d}z = \hat{\mathbf{q}}^H\mathbf{Q}\hat{\mathbf{q}}, \tag{8}$$

where $\mathbf{Q}$ is the energy weight matrix that contains the appropriate weighting of the variables at the collocation points, as well as the integration weights between the channel walls. A Cholesky decomposition of $\mathbf{Q} = \mathbf{F}^H\mathbf{F}$ allows us to relate this norm to an equivalent standard (Euclidean) L_2-norm $||\hat{\mathbf{q}}||_E = ||\mathbf{F}\hat{\mathbf{q}}||_2$. The energy norm of a matrix $\mathbf{A}$ is easily derived using the definition of a vector-induced norm

$$||\mathbf{A}||_E = \max_{\hat{\mathbf{q}}\neq 0}\frac{||\mathbf{A}\hat{\mathbf{q}}||_E}{||\hat{\mathbf{q}}||_E} = \max_{\hat{\mathbf{q}}\neq 0}\frac{||\mathbf{F}\mathbf{A}\mathbf{F}^{-1}\mathbf{F}\hat{\mathbf{q}}||_2}{||\mathbf{F}\hat{\mathbf{q}}||_2} = ||\mathbf{F}\mathbf{A}\mathbf{F}^{-1}||_2 = \sigma_{max}(\mathbf{F}\mathbf{A}\mathbf{F}^{-1}), \tag{9}$$

where σ_{max} is the largest singular value of the matrix. In order to study the receptivity of the system, we calculate the maximum energy amplification of the output with respect to the input, optimized over all shapes of the input forcing

$$\mathcal{R}(\alpha, \beta, \omega) = \max_{\hat{\mathbf{f}}\neq 0}\frac{||\hat{\mathbf{y}}||_E}{||\hat{\mathbf{f}}||_E} = \max_{\hat{\mathbf{f}}\neq 0}\frac{||\mathcal{H}(\alpha, \beta, \omega)\hat{\mathbf{f}}||_E}{||\hat{\mathbf{f}}||_E} = ||\mathcal{H}(\alpha, \beta, \omega)||_E. \tag{10}$$

Hence, the response of the system is measured as the energy norm of the transfer function. Subsequently, the componentwise response is defined as the energy norm of the componentwise transfer function, i.e., $\mathcal{R}_{xs}(\alpha, \beta, \omega) = ||\mathcal{H}_{xs}(\alpha, \beta, \omega)||_E$. The response maximized over all temporal frequencies is known in literature as the $\mathcal{H}_\infty$-norm and can be interpreted as the worst case amplification of deterministic inputs [30].

$$||\mathcal{H}_{xs}||_\infty(\alpha, \beta) = \max_{\omega}\mathcal{R}_{xs}(\alpha, \beta, \omega). \tag{11}$$

Eq. (11) shows how we calculate the componentwise $\mathcal{H}_\infty$-norm.

2.3.2. Modal decomposition and order reduction

Before we can compute $\mathcal{R}_{xs}(\alpha, \beta, \omega)$ from the above expressions, we have to perform a modal decomposition of the dynamics operator $\mathbf{L} = \mathbf{V}\mathbf{\Lambda}\mathbf{V}^{-1}$. Here, $\mathbf{V}$ is the matrix whose columns are the

eigenvectors of $\mathbf{L}$, and $\mathbf{\Lambda}$ is a diagonal matrix containing its eigenvalues. This way, the resolvent operator in Eq. (7) becomes $\mathbf{C}(i\omega\mathbf{I}-\mathbf{L})^{-1}\mathbf{B} = \mathbf{C}\mathbf{V}(i\omega\mathbf{I}-\mathbf{\Lambda})^{-1}\mathbf{V}^{-1}\mathbf{B}$, which now only requires inverting a diagonal matrix instead of a full one.

Using N collocation points, the length of the state vector $\hat{\mathbf{q}} = (\hat{w}, \hat{\eta}, \hat{\tau})^T$ is $3N-6$ (since it does not include the domain boundaries), and therefore computing the eigenvalues and eigenfunctions requires $O((3N-6)^3)$ arithmetic operations. To reduce the amount of computational work, we restrict our attention to the K least stable modes instead of all $3N-6$, thus requiring only $O(K^3)$ operations [31,25].

3. Experimental methods

3.1. Device fabrication

A swirl flow minichannel heat sink is fabricated in order to assess the validity of the numerical base flow results, and to study the influence of a pulsating flow rate on the thermal performance. The device consists of two parts: a thermally insulating body made from nylon thermoplastic, where the channel was manufactured using conventional lathe and mill techniques; and a thermally conductive cover made from a 6061 aluminum sheet used as the heat exchange surface. Inlet and outlet ports were machined in the body, as well as a feeder channel, holes for screws and a groove for the o-ring used to seal the two pieces. A disassembled view of the fabricated device is shown in Fig. 2.

The feeder channel is 12.7 mm deep and 3.18 mm wide, and is designed to get a flow inlet angle $\theta = 4°$. The most important dimensions of the fabricated swirl flow minichannel heat sink are shown in Table 1.

3.2. Experimental equipment and instrumentation

Water is pumped from a reservoir and through a Vinyl tubing closed loop using a Cole-Parmer® gear pump. A needle valve and an in-line flowmeter (both Cole-Parmer®) are used to regulate and measure the flow rate. An Omega™ ultra-thin heat sheet with an output of 250 W is attached to the aluminum cover of the minichannel to act as a heat source. Hot water leaving the heat sink goes through a finned coil heat exchanger, there heat is rejected to the ambient air via forced convection using fans, water cools down and then it returns to the reservoir. A pulsating flow generator was built to superimpose a pulsating flow rate over the mean flow provided by the gear pump. The mechanism of this actuator consists in periodically squeezing the Vinyl tubing before the inlet of the heat sink, and this is achieved using a 200 rpm and 12VDC motor to drive a wheel that has rods attached to it. These rods are parallel to the axis of the wheel but are eccentric, therefore pressing and releasing the tubing on every rotation cycle. Fig. 3 shows the main components of the experimental setup and the wheels with different number of rods that are used to generate pulsations at different frequencies.

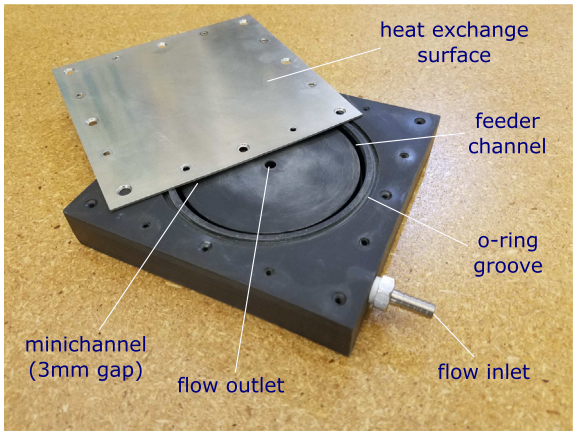

Fig. 2. Disassembled view of the fabricated device.

Table 1
Dimensions of the fabricated device.

h	r_o	r_i	θ_0
1.5 mm	50 mm	3.18 mm	4°

An in-line flowmeter from Cole-Parmer® is used for a direct reading of the flow rate. The pressure drop in the minichannel is measured using two Cole-Parmer® high-accuracy pressure transducers and the inlet and outlet flow temperatures are measured using K-type thermocouples. National Instruments™ data acquisition systems (DAQs) along with the Labview software were used for both, pressure and flow temperature measurements. In order to estimate the inside wall temperature in the minichannel, we measure temperature at the center of the exposed side of the ultra-thin heat sheet using a Flir™ spot thermal camera with a tripod. The range and accuracy of the instrumentation used for the experiments are shown in Table 2, this excludes the range and resolution of the DAQs which was taken into account in the uncertainty analysis.

3.3. Testing procedure

Inlet and outlet flow temperatures, surface temperature, and pressure drop in the minichannel were registered simultaneously for a range of flow rates with and without pulsations at different frequencies. The procedure started by turning on the pump and heater and letting the system run for 25 min, until the closed loop reached a thermal steady state. Throughout the testing, room temperature was maintained between 20 and 22 °C. Pressure drop and flow temperatures were recorded over a period of 5s, and the surface temperature reading was annotated. The flow rate was lowered and new measurements were taken after the temperature fluctuations were smaller than 0.5 °C/min. Once the minimum flow rate was reached, the needle valve was fully opened again, and the procedure was repeated with the pulsating flow generator turned on, and for each of the of four different wheels that give different pulsating frequencies. Therefore, the data set is composed of measurements at 17 different flow rates for each of the 6 pulsating frequencies (including no pulsations). Results presented in this article are the average of three series of data sets.

3.4. Experimental calculations

For each flow rate and pulsating frequency, the pumping power $\dot{\mathcal{W}}$, the average wall heat flux q''_w, the wall temperature at the inside of the minichannel T_w, and the Nusselt number Nu were calculated as follows

$$\dot{\mathcal{W}} = \dot{V}\Delta p, \tag{12}$$

$$q''_w = \frac{\rho C_p \dot{V}(T_{out} - T_{in})}{\pi(r_o^2 - r_i^2)}, \tag{13}$$

$$T_w = T_{top} - \frac{q''_w}{R_{th}}, \tag{14}$$

$$Nu = \frac{q''_w d_h}{\kappa(T_w - T_{av})}, \tag{15}$$

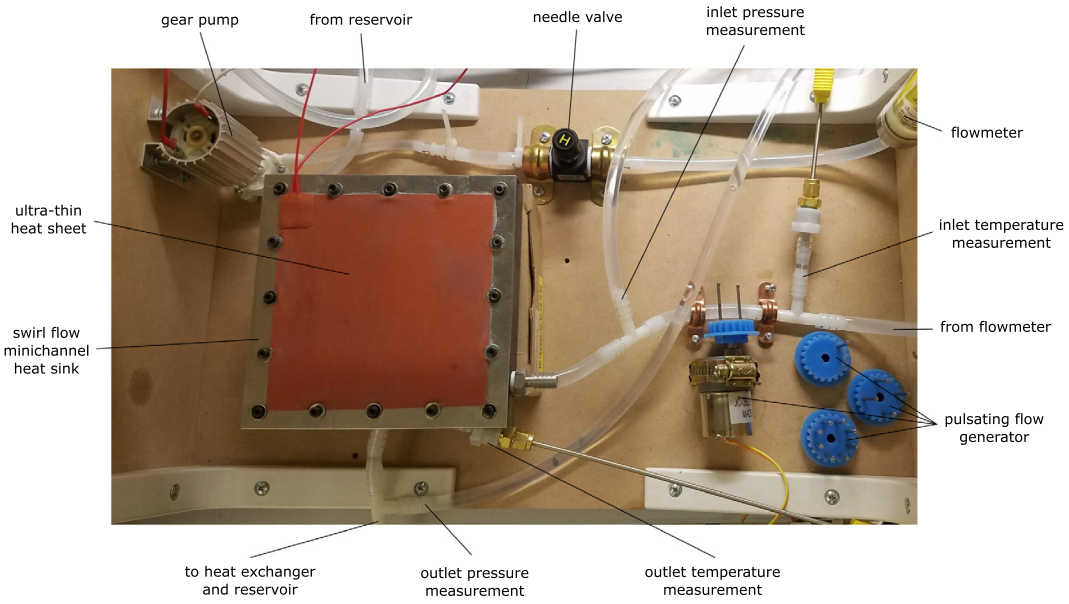

Fig. 3. Main components in experimental setup.

Table 2
Instrumentation range and accuracy.

Measurement	Device range	Accuracy
Flow rate	0.4–4 l/min	5%
Pressure	0–345 kPa	0.86 kPa
Flow temperature	−200–1250 °C	Greater of 1.1 °C or 0.4%
Surface temperature	−25–380 °C	Greater of 1.5 °C or 1.5%

where $\dot{V}$ is the volume flow rate, Δp is the root mean square (RMS) of the total pressure drop signal, r_i and r_o are the inner and outer radius respectively, T_{in}, T_{out} and T_{av} correspond to the flow temperatures measured at the inlet of the channel, at the outlet, and the average between both, T_{top} is the surface temperature measured from the outside, R_{th} is the conductive thermal resistance of the aluminum cover, d_h is the hydraulic diameter taken as twice the channel height, and C_p and κ are the heat capacity and thermal conductivity of water, respectively.

Uncertainty of the measured quantities is calculated using the instrumentation information shown in Table 2, as well as the range and resolution of the data acquisition systems. Systematic uncertainty of the flow temperature difference $T_{out} - T_{in}$ is eliminated by zeroing the measurement of both thermocouples using the same reference. Uncertainty is propagated from the measurements to the calculated variables q''_w, T_w and Nu using the Taylor series method.

$$e^2_{f(x_1,\ldots c,x_n)} = \sum_{i=1}^{n}\left(\frac{df}{dx_i}e_{x_i}\right)^2. \tag{16}$$

Eq. (16) shows how we compute the uncertainty e_f for a calculated variable f which depends on measurements $x_1, \ldots c, x_n$, each with uncertainty e_{x_i}.

4. Results and discussion

4.1. Steady state performance and base flow

Performance of the swirl flow minichannel heat sink for flow rates between 0.43 and 1.12 l/min without pulsations is presented in this section. The flow rate Reynolds number is calculated as $Re_o = \dot{V}h/(8\pi v r_o^2)$, where the viscosity is evaluated at film temperature $T_{film} = (T_o + T_w)/2$. Experimental results for the total pressure drop, wall temperature and Nusselt number as a function of Re_o, for the range allowed by the experimental setup, are shown in Fig. 4.

Numerical results are also shown in Fig. 4 for flow rate Reynolds numbers up to $Re_o^c = 0.91$, where the steady state solution predicts

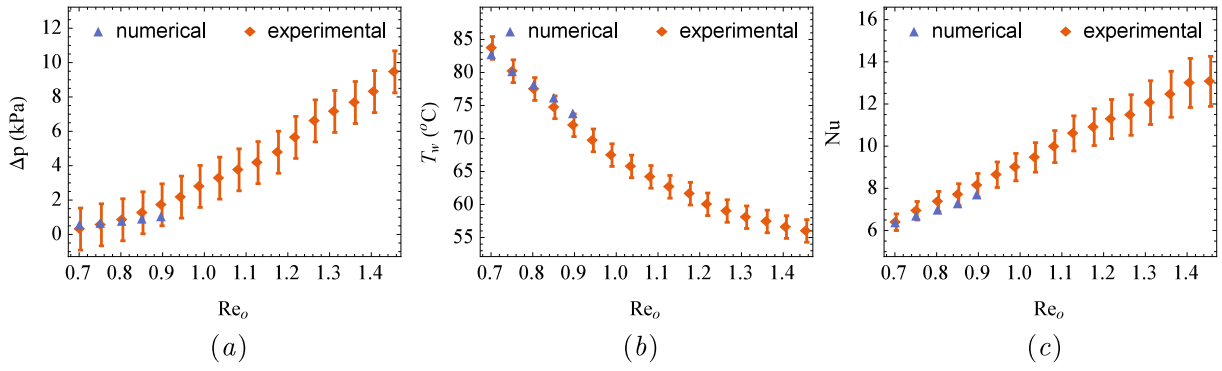

Fig. 4. Numerical and experimental heat sink performance variables as a function of the flow rate Reynolds number. (*a*) Total pressure drop. (*b*) Wall temperature. (*c*) Nusselt number.

a change in the boundary layer structure from parabolic to inflected velocity profiles. At the same time, for flow rate Reynolds numbers greater than this, we find eigenvalues of the **L** operator with positive real part, therefore the linearized perturbation equations predict the onset of asymptotic instability at this same critical value Re_o^c. Although the present experiments were not designed to determine the presence of instabilities, flow visualization experiments were carried out by Ruiz and Carey in Ref. [15] using dye injection. They observed the onset of unsteadiness and a significant increase in dye diffusion when the flow rate going through the channel exceeded 190 ml/min, which corresponds to $Re_o = 0.86$ according to our definition of the flow rate Reynolds number. Therefore, the onset of transition predicted by the present theoretical analysis is consistent with experimental observations. Pressure ports in the present experiment are not located at the inlet and outlet of the minichannel section that corresponds to the computational domain of the numerical simulations. Therefore, the numerical values of Δp shown in Fig. 4. (*a*) consider the pressure drop from the simulations, as well as losses that take place between the pressure ports and the computational domain. These losses are calculated using typical models found in literature such as Refs. [32,33], and include friction losses in the tubing and the feeder channel, a sudden expansion at the inlet, a sudden contraction and a 90° bend at the outlet, and the fittings.

As shown in Fig. 4, reasonable agreement is found between the numerical and experimental results for $Re_o < Re_o^c$, thus validating the base flow that is used in the next section to carry out the componentwise receptivity analysis. This base flow corresponds to the numerical solution for $Re_o = 0.9$ ($\dot{V} = 603$ ml/min) evaluated at a local radius r. As discussed in Ref. [16], the overall behaviour of the base flow does not depend strongly on the local radius, therefore we arbitrarily select $r = 0.4r_o$ as a representative local radius for the dynamics in the swirl flow minichannel heat sink. Although our conclusions in this study are not affected by this particular value, we consider that a global stability approach is a logical next step for future work.

Table 3 shows the parameters that govern the local base flow: the local Reynolds number *Re* based on the half-height of the channel and the streamwise velocity component $\sqrt{U^2 + V^2}$ at $z = 0$, the Prandtl number *Pr*, and the local flow angle at the midplane of the channel θ_c, measured starting from the tangential direction.

4.2. Componentwise response

In this section we present our results and analysis of the componentwise response of the base flow $\mathcal{R}_{xs}$ and its dependence on the wavevector and temporal frequency. In order to study the influence of the wavevector, instead of using its radial and azimuthal components α and β, we use its magnitude $k = \sqrt{\alpha^2 + \beta^2}$ and the waveangle defined as $\theta_k = \arctan(\alpha/\beta) - \theta_c$. In this notation, an angle $\theta_k = 0$ represents a wave propagating in the direction of flow in the midplane of the channel (aligned with θ_c), which we refer to as the streamwise direction. Therefore, we refer to $\theta_k = \pi/2$ as the crossflow direction, and it represents a wave direction normal to the flow at $z = 0$.

A mesh sensitivity analysis is carried out to select the number of Chebyshev collocation points *N* used to discretize in the *z* direction. Table 4 shows the real and imaginary parts of the 10^{th} eigenvalue of **L** for $k = 1$ and $\theta_k = 0$. We use $N = 120$ collocation points, as it is sufficient resolution to get convergence of up to 8 digits.

Table 3
Local base flow parameters for $Re_o = 0.9$ at $r = 0.4r_o$.

Re	*Pr*	θ_c
200.97	3.41	32.17°

Table 4
Mesh sensitivity of the 10^{th} eigenvalue for $k = 1$ and $\theta_k = 0$.

N	$\mathrm{Re}(\lambda_{10})$	$\mathrm{Im}(\lambda_{10})$
20	−0.20314397	−0.36092704
60	−0.20335108	−0.36428062
120	−0.20335107	−0.36428062
200	−0.20335107	−0.36428062

To reduce the computational cost, the state vector $\hat{\mathbf{q}}$ is represented as an eigenfunction expansion using only *K* modes instead of all $3N - 6$. The response to radial forcing $\mathcal{R}_{u\tau}$ for $k = 10, \theta_k = 0$ and $\omega = 0$ is calculated for different values of *K*. As shown in Fig. 5, a modal truncation using $K = 180$ modes is enough to get accurate results.

The componentwise response of the system is calculated for wavenumbers between $k = 0.01$ and 6, and waveangles varying from the azimuthal direction ($\theta_k = -32.17° \approx -\pi/6$) to the crossflow direction ($\theta_k = \pi/2$). Results for different values of the temporal frequency ω are shown in Figs. 6(*a*), 7(*a*) and 8(*a*), for a forcing in the radial, azimuthal and wall-normal momentum components, respectively. Our results for the componentwise $\mathcal{H}_\infty$-norm (response maximized over all ω) are shown in Figs. 6(*b*), 7(*b*) and 8(*b*), for radial, azimuthal and wall-normal momentum forcing respectively.

Temperature perturbations are most amplified by streamwise independent structures, i.e., streamwise vortices and streaks ($\theta_k = \pi/2$), as shown in Figs. 6(*b*), 7(*b*) and 8(*b*). The maximum response is of order $O(10^3)$ for all forcing components, where the largest amplification corresponds to radial, then wall-normal, and then azimuthal forcing. These largest amplifications occur for a forcing frequency $\omega = 0$ and, as ω increases, the maximum response decreases and oblique (spiral) waves become the most amplified structures, as shown in Figs. 6(*a*), 7(*a*) and 8(*a*). Increasing ω further, the dominant structures become axisymmetric inward traveling waves ($\theta_k = -\theta_c + \pi/2 \approx \pi/3$) with an amplification of order $O(10^2)$. At even higher frequencies, amplifications are of order $O(10)$ and, azimuthally propagating waves ($\theta_k = -\theta_c \approx -\pi/3$) dominate for azimuthal forcing, while for radial and wall-normal forcing the dominant structures are streamwise propagating waves ($\theta_k = 0$), which we interpret as the spiral analog to T-S waves.

The results presented above are useful for developing heat transfer enhancement strategies, as we now know what are the flow structures that generate the largest response in the temperature field for a given range of excitation frequencies.

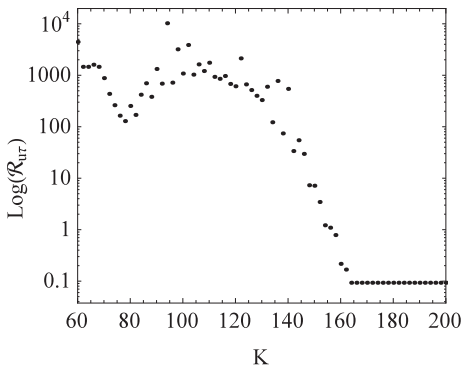

Fig. 5. Response to radial forcing $\mathcal{R}_{u\tau}$ for $k = 10, \theta_k = 0$ and $\omega = 0$ calculated using *K* modes.

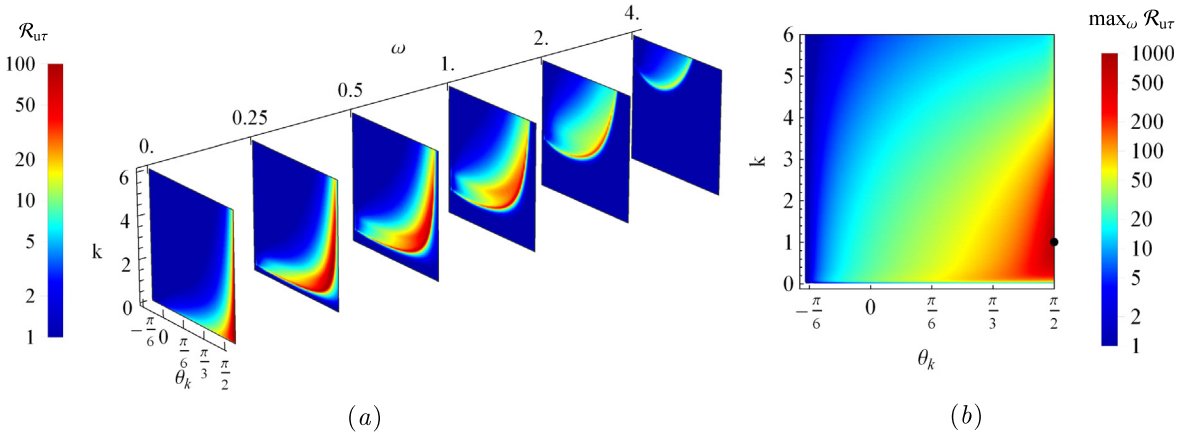

Fig. 6. Response to radial momentum forcing $\mathcal{R}_{u\tau}$ as a function of the total wavenumber k and the waveangle θ_k. (a) Slices for different values of the temporal frequency ω. (b) Response maximized over all ω. The largest response is indicated by a black dot.

4.3. Heat transfer enhancement strategies

In order to develop a feasible heat transfer enhancement strategy, many practical considerations have to be taken into account. An actuator has to be designed that is able to excite waves that propagate in a particular direction for a specific range of forcing frequencies. It is also desired that the actuator is easy to manufacture and to integrate with the heat sink design. With this in mind, we will propose and discuss two strategies to enhance heat transfer with distinct objectives: (1) maximum amplification, and (2) simple implementation.

From Figs. 6–8 we know that the maximum amplification is obtained for crossflow stationary waves with $\omega = 0$ (streamwise independent structures). In order to excite said structures, we propose micromachining the channel walls with spiral grooves that follow the predicted streamlines of the base flow. These grooves should be spatially periodic in the crossflow direction with a wavelength corresponding to the wavenumber that provides the largest amplification. The passive actuation is expected to generate streamwise independent perturbations of the base flow in the wall-normal direction, therefore, in order to study the response to this type of forcing, we calculate $\mathcal{R}_{w\tau}$ for $\theta_k = \pi/2$, which is shown in Fig. 9.

Large amplifications are obtained for a narrow range of forcing frequencies concentrated around $\omega = 0$, and the maximum response occurs for $k = 1.61$, as shown in Fig. 9(a). Structures of different wavenumbers dominate for every frequency excited, therefore the response to the actuation is given by the amplification maximized over all k, that is, the envelope of the frequency response for all k, as shown in Fig. 9(b).

As a second heat transfer enhancement strategy, we propose using a pulsating flow rate, which can be achieved using the actuator described in Section 3.2. Implementation of this strategy is very simple, as it does not require any modifications to the heat sink design. Using a pulsating flow rate results in an oscillating perturbation of the pressure gradient, and therefore a forcing in the radial momentum component. Pulsations are generated in the tubing upstream of the minichannel, hence we expect only streamwise propagating perturbations to reach the device. Consequently in order to study the response to this type of forcing, we calculate $\mathcal{R}_{u\tau}$ for $\theta_k = 0$, which is shown in Fig. 10.

Moderate amplifications are obtained for a wide range of forcing frequencies, and the maximum response occurs for $k = 0.11$ at $\omega = 0.10$, as shown in Fig. 10(a). As the forcing frequency increases, the largest response is obtained for a larger wavenumber, hence for a shorter wavelength. The response to the pulsating flow rate is given by the amplification maximized over all k, that is, the envelope of the frequency response for all k, as shown in Fig. 10 (b).

It is important to remark that, the strategies here presented are based on the fact that a large temperature response to a momentum forcing suggests a heat transfer enhancement, but nothing

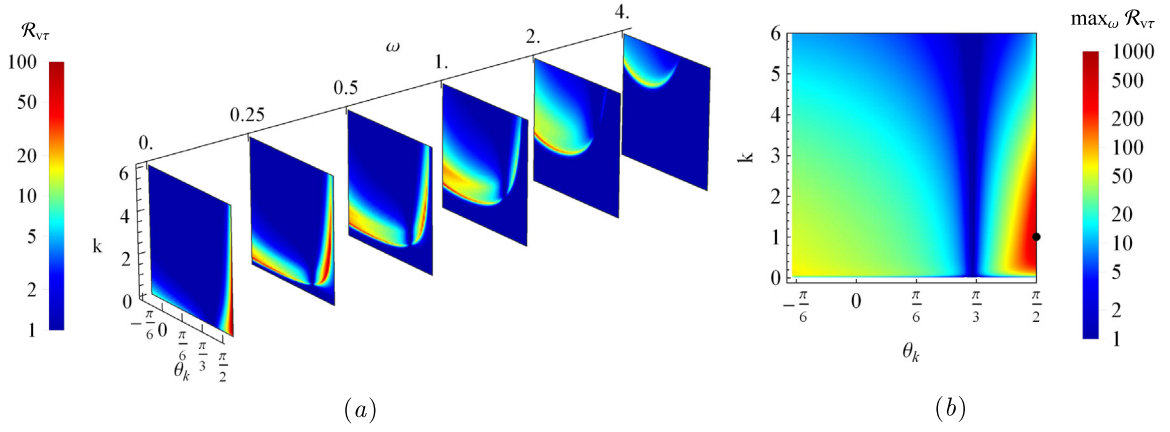

Fig. 7. Response to azimuthal momentum forcing $\mathcal{R}_{v\tau}$ as a function of the total wavenumber k and the waveangle θ_k. (a) Slices for different values of the temporal frequency ω. (b) Response maximized over all ω. The largest response is indicated by a black dot.

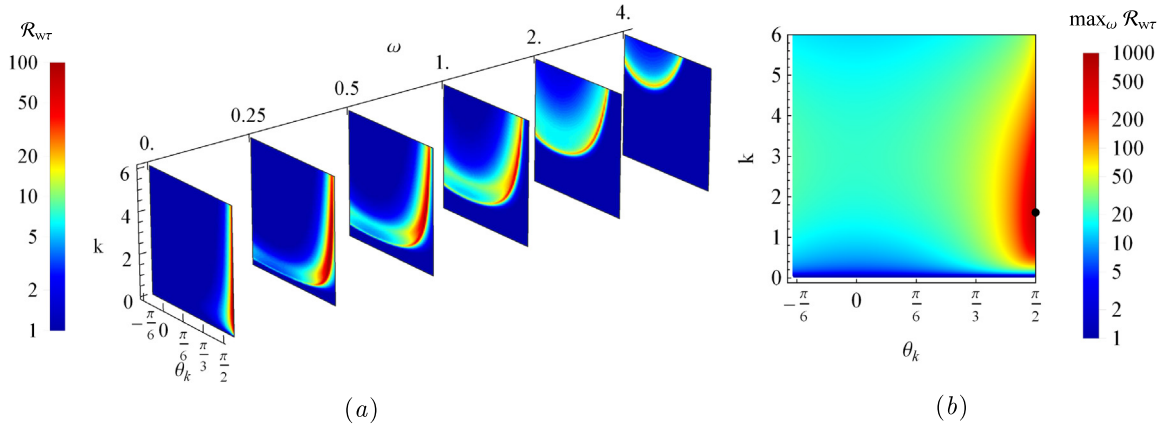

Fig. 8. Response to wall-normal momentum forcing $\mathcal{R}_{w\tau}$ as a function of the total wavenumber k and the waveangle θ_k. (a) Slices for different values of the temporal frequency ω. (b) Response maximized over all ω. The largest response is indicated by a black dot.

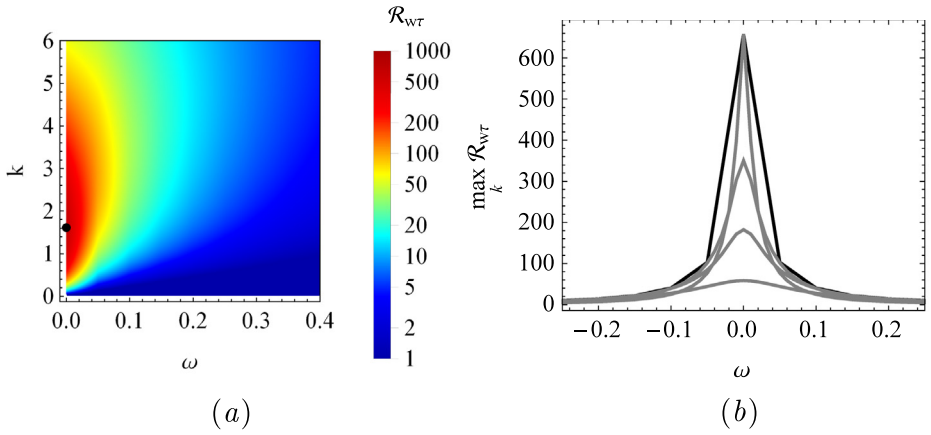

Fig. 9. Response to wall-normal forcing of crossflow waves ($\theta_k = \pi/2$). (a) Response as a function of the total wavenumber k and temporal frequency ω. The maximum amplification is marked with a black dot. (b) Response maximized over all wavenumbers in black, and for selected wavenumbers in gray.

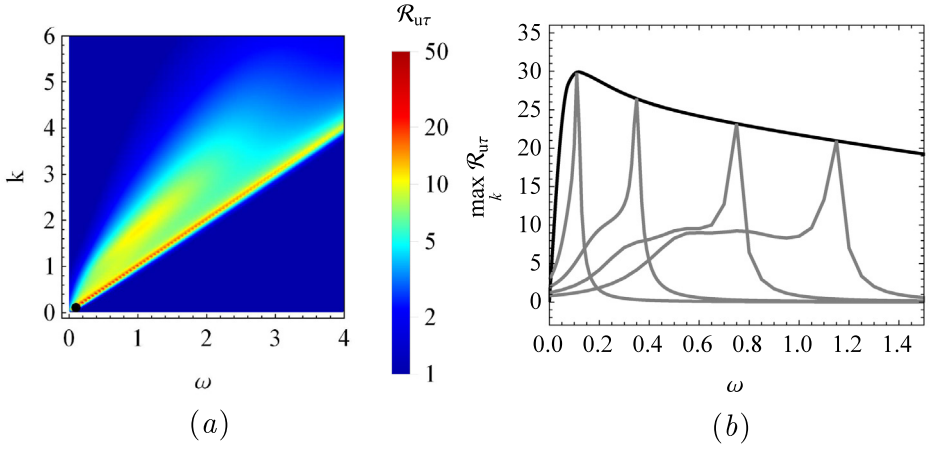

Fig. 10. Response to radial forcing of streamwise propagating waves ($\theta_k = 0$). (a) Response as a function of the total wavenumber k and temporal frequency ω. The maximum amplification is marked with a black dot. (b) Response maximized over all wavenumbers in black, and for selected wavenumbers in gray.

has been said about the kinetic energy loss that may be associated with it. This may result in a higher pressure drop across the channel, and consequently an undesired heat sink performance. Experimental results for the performance of the swirl flow minichannel heat sink with a pulsating flow rate are presented in the next section. Based on the receptivity analysis, the channel with streamwise and spiral grooves should be a more efficient strategy for enhancing heat transfer. Nevertheless, testing this hypothesis

experimentally requires manufacturing several devices, therefore it will be investigated in future work. In addition to the strategies here discussed, other more sophisticated techniques may be implemented using the information provided by the receptivity analysis, such as blowing and suction, vortex generators, or acoustic excitation.

4.4. Case study: pulsating flow rate

Experimental results of the heat sink performance using a pulsating flow rate are presented in this section as a proof of concept. As explained in the previous subsection, flow pulsations result in a streamwise propagating disturbance of the radial momentum component. The range of pulsation frequencies used in the experiments is selected based on the range of frequencies for which large amplification of disturbances is predicted by the componentwise receptivity analysis, as shown in Fig. 10(*b*). The actuator described in Section 3.2 is used with a different number of rods to generate pulsations with frequencies of 1.67, 3.33, 6.67, 13.33, and 26.67 s^{-1}. These correspond to the dimensionless angular frequencies $\omega = 0.22,\ 0.44,\ 0.88,\ 1.76$ and 3.52, based on the scales used for the receptivity analysis. The RMS pressure drop, wall temperature and Nusselt number present a similar behavior for all frequencies, and the largest response is observed for $\omega = 0.88$, which is shown in Fig. 11.

Fig. 11(*a*) shows that the pulsations slightly increase the total pressure drop, and this effect becomes accentuated for lower flow rate Reynolds numbers. On the other hand, for the same Re_o, the wall temperature is noticeably reduced by the actuation, with up to a 5 °C difference for the lowest flow rate tested, as shown in Fig. 11(*b*). Because the heat input to the system is unchanged, this means that convective heat transfer is being enhanced, as evidenced by the measurements of the Nusselt number shown in Fig. 11(*c*). This occurs because of increased mixing due to the unsteadiness provided by the flow pulsations, resulting in a more homogeneous wall-normal temperature distribution.

In order to assess if the changes in performance using a pulsating flow rate are desirable, we calculate the following indicators: (1) the reduction in the pumping power required to achieve the same wall temperature as in the unforced case, and (2) the enhancement of the Nusselt number using the same pumping power as in the unforced case. These indicators are shown in Fig. 12 as a function of the pulsation frequency for $Re_o = 0.99$.

According to Fig. 12(*a*), in order to achieve a specific wall temperature requirement, up to 26.6% less pumping power is needed when using a pulsating flow rate. If the same pumping power is used, an increment of up to 10.3% in the Nusselt number is observed with the actuation, as shown in Fig. 12(*b*). The experimental response curves to a pulsating flow rate, Fig. 12, resemble the result obtained from the receptivity analysis in Fig. 10(*b*), where a maximum is obtained for a relatively low frequency, and then the amplification slowly decays for higher frequencies.

These results are promising, since the receptivity analysis suggests that an even larger response should be observed for other types of forcing. However, a better heat sink performance is not guaranteed, as the pumping cost penalty may be greater than the benefit of increasing the convective heat transfer.

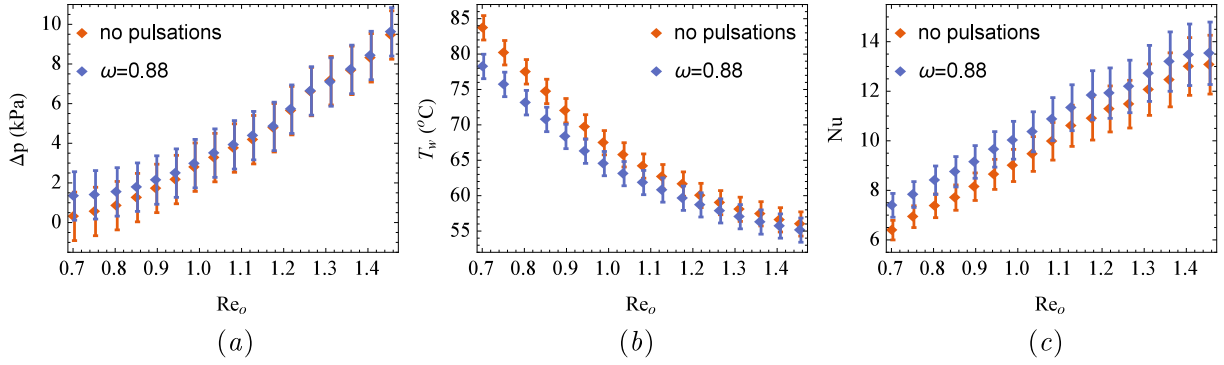

Fig. 11. Experimental heat sink performance variables as a function of the flow rate Reynolds number with and without forcing. (*a*) Total pressure drop. (*b*) Wall temperature. (*c*) Nusselt number.

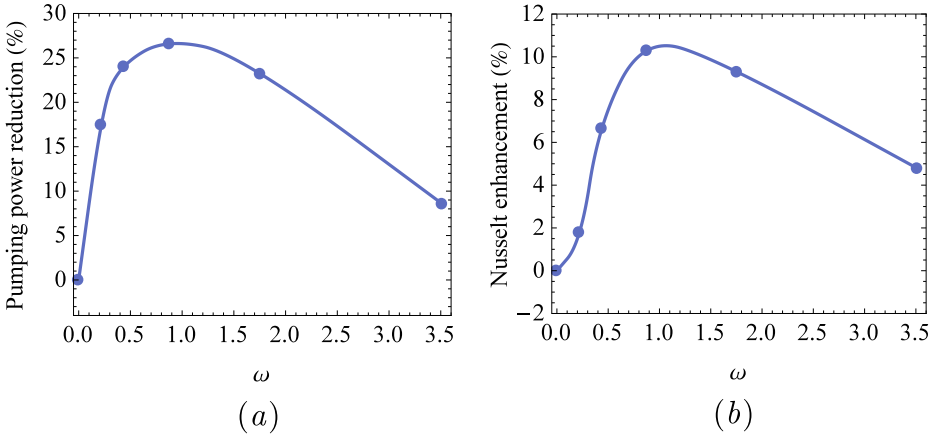

Fig. 12. Heat sink performance response to actuation as a function of the pulsation frequency ω for a flow rate Reynolds number $Re_o = 0.99$. (*a*) Pumping power reduction to achieve the same wall temperature. (*b*) Nusselt enhancement at the same pumping power.

5. Conclusions

This study presents a theoretical and numerical analysis of the input-output response of temperature disturbances to forcing of the momentum components in a swirl flow channel heat sink. The steady state flow is solved using methods previously reported in Refs. [16,17]. The device is fabricated and experiments are conducted to measure the performance curves of the heat sink, that is, pressure drop and wall temperature as a function of flow rate for a given heat flux. Experimental results agree with numerical calculations for subcritical Reynolds numbers, therefore validating the base flow. Linearized perturbation equations with harmonic forcing are obtained using the local and parallel flow approximations based on order of magnitude arguments.

The amplification of temperature perturbations to forcing of the radial, azimuthal, and wall-normal momentum components is calculated for a range of wavenumbers, waveangles and temporal frequencies. The most amplified spatial structures are streamwise vortices and streaks with a maximum response of order $O(10^3)$ for $\omega = 0$. As the forcing frequency increases, the dominant structures change their propagating direction, from crossflow to oblique to axisymmetric radial waves with amplification of order $O(10^2)$. At higher frequencies, streamwise propagating waves dominate for radial or wall-normal forcing, and azimuthally propagating waves dominate for azimuthal forcing, in both cases with amplifications of order $O(10)$.

Excitation of streamwise independent structures gives the largest amplification of temperature disturbances, it is therefore an attractive strategy to enhance heat transfer. To achieve this, we propose micromachining the channel walls with spiral grooves aligned with the predicted streamlines of the base flow. The response curve to this type of forcing shows that large amplifications occur for a narrow range of frequencies concentrated around $\omega = 0$. Excitation of streamwise propagating waves results in only moderate amplification of temperature disturbances. Nonetheless, in order to generate these perturbations, we propose using a pulsating flow rate as a heat transfer enhancement technique due to its simple implementation. The response curve to this type of forcing shows a wide range of actuation frequencies with similar gains.

Heat sink performance using a pulsating flow rate is measured experimentally for the range of frequencies provided by the receptivity analysis. Compared to the unforced case, the RMS pressure drop is slightly higher, specially for low flow rates, and the wall temperature decreases significantly, with a difference of up to 5 °C. In order to evaluate if the heat sink performance with pulsations is better than the performance in the unforced case, we calculate the pumping power reduction to get the same wall temperature, and the Nusselt enhancement using the same pumping power. A pumping power reduction of up to 26.6% was observed, along with a Nusselt enhancement of up to 10.3%.

In this work, a significant performance improvement for the swirl flow channel heat sink was achieved using a pulsating flow rate. Actuation parameters, in this case the range of pulsation frequencies, were determined by the receptivity analysis. This physics based approach can be extended to other heat transfer enhancement techniques, for instance, to select the wavelength of a wavy surface, the periodicity of surface roughness elements, or the frequency of acoustic vibrations.

Conflict of Interest

We confirm that there are no known conflicts of interest associated with this publication and there has been no financial support for this work that has influenced its outcome.

Acknowledgements

B. H-P. thanks CONICYT- Chile for his Ph.D. scholarship CONICYT-PCHA/Doctorado Nacional/2015-21150139. The authors would also like to thank V. Plotnikov and A. Muñoz-Hernandez for their help with the experimental setup, and B. Zimmermann for machining the parts of the minichannel heat sink.

References

[1] S.G. Kandlikar, W.J. Grande, Evaluation of single phase flow in microchannels for high heat flux chip cooling–thermohydraulic performance enhancement and fabrication technology, Heat Transfer Eng. 25 (8) (2004) 5–16.
[2] M. Datta, H.-W. Choi, Microheat exchanger for cooling high power laser diodes, Appl. Therm. Eng. 90 (2015) 266–273.
[3] A. Royne, C. Dey, D. Mills, Cooling of photovoltaic cells under concentrated illumination: a critical review, Sol. Energy Mater. Sol. Cells 86 (4) (2005) 451–483.
[4] J. Osses-Márquez, W.R. Calderón-Muñoz, Thermal influence on charge carrier transport in solar cells based on GaAs PN junctions, J. Appl. Phys. 116 (15) (2014) 154502.
[5] W.R. Calderón-Muñoz, C. Jara-Bravo, Hydrodynamic modeling of hot-carrier effects in a PN junction solar cell, Acta Mech (2016) 1–14.
[6] B. Agostini, M. Fabbri, J.E. Park, L. Wojtan, J.R. Thome, B. Michel, State of the Art of High Heat Flux Cooling Technologies, Heat Transfer Eng. 28 (4) (2007) 258–281.
[7] S.G. Kandlikar, A.V. Bapat, Evaluation of jet impingement, spray and microchannel chip cooling options for high heat flux removal, Heat Transfer Eng. 28 (11) (2007) 911–923.
[8] A.C. Kheirabadi, D. Groulx, Cooling of server electronics: a design review of existing technology, Appl. Therm. Eng. 105 (2016) 622–638.
[9] M.E. Steinke, S.G. Kandlikar, Review of single-phase heat transfer enhancement techniques for application in microchannels, minichannels and microdevices, Int. J. Heat Technol. 22 (2) (2004) 3–11.
[10] M. Meis, F. Varas, A. Velázquez, J. Vega, Heat transfer enhancement in microchannels caused by vortex promoters, Int. J. Heat Mass Transf. 53 (1) (2010) 29–40.
[11] L. Léal, M. Miscevic, P. Lavieille, M. Amokrane, F. Pigache, F. Topin, B. Nogarède, L. Tadrist, An overview of heat transfer enhancement methods and new perspectives: focus on active methods using electroactive materials, Int. J. Heat Mass Transf. 61 (2013) 505–524.
[12] A. Dewan, P. Srivastava, A review of heat transfer enhancement through flow disruption in a microchannel, J. Therm. Sci. 24 (3) (2015) 203–214.
[13] N.A.C. Sidik, M.N.A.W. Muhamad, W.M.A.A. Japar, Z.A. Rasid, An overview of passive techniques for heat transfer augmentation in microchannel heat sink, Int. Commun. Heat Mass Transfer 88 (2017) 74–83.
[14] M. Ruiz, V.P. Carey, Prediction of Single Phase Heat and Momentum Transport in a Spiraling Radial Inflow Microchannel Heat Sink, ASME, 2012, Paper No. HT2012-58328.
[15] M. Ruiz, V.P. Carey, Experimental study of single phase heat transfer and pressure loss in a spiraling radial inflow microchannel heat sink, J. Heat Transfer 137 (7) (2015) 071702.
[16] B. Herrmann-Priesnitz, W.R. Calderón-Muñoz, E.A. Salas, A. Vargas-Uscategui, M.A. Duarte-Mermoud, D.A. Torres, Hydrodynamic structure of the boundary layers in a rotating cylindrical cavity with radial inflow, Phys. Fluids 28 (3) (2016) 033601.
[17] B. Herrmann-Priesnitz, W.R. Calderón-Muñoz, A. Valencia, R. Soto, Thermal design exploration of a swirl flow microchannel heat sink for high heat flux applications based on numerical simulations, Appl. Therm. Eng. 109 (2016) 22–34.
[18] N. Gregory, J.T. Stuart, W.S. Walker, On the stability of three-dimensional boundary layers with application to the flow due to a rotating disk, Phil. Trans. R. Soc. Lond. 248 (943) (1955) 155–199.
[19] M.R. Malik, The neutral curve for stationary disturbances in rotating-disk flow, J. Fluid Mech. 164 (1986) 275287.
[20] R.J. Lingwood, Absolute instability of the boundary layer on a rotating disk, J. Fluid Mech. 299 (1995) 17–33.
[21] E. Serre, E.C. del Arco, P. Bontoux, Annular and spiral patterns in flows between rotating and stationary discs, J. Fluid Mech. 434 (2001) 65100.
[22] J.M. Lopez, F. Marques, A.M. Rubio, M. Avila, Crossflow instability of finite Bödewadt flows: transients and spiral waves, Phys. Fluids 21 (11) (2009) 114107.
[23] Y. Do, J.M. Lopez, F. Marques, Optimal harmonic response in a confined Bödewadt boundary layer flow, Phys. Rev. E 82 (3) (2010) 036301.
[24] L.N. Trefethen, A.E. Trefethen, S.C. Reddy, T.A. Driscoll, Hydrodynamic stability without eigenvalues, Science 261 (5121) (1993) 578–584.
[25] P.J. Schmid, D.S. Henningson, Stability and Transition in Shear Flows, Springer Verlag, New York, 2001.
[26] P.J. Schmid, Nonmodal stability theory, Annu. Rev. Fluid Mech. 39 (1) (2007) 129–162.

[27] P.J. Schmid, L. Brandt, Analysis of fluid systems: stability, receptivity, sensitivity, Appl. Mech. Rev. 66 (2) (2013) 024803.
[28] M.R. Jovanović, B. Bamieh, Componentwise energy amplification in channel flows, J. Fluid Mech. 534 (2005) 145183.
[29] L.H. Gustavsson, Excitation of direct resonances in plane Poiseuille flow, Stud. Appl. Math. 75 (3) (1986) 227–248.
[30] K. Zhou, J.C. Doyle, K. Glover, et al., Robust and Optimal Control, vol. 40, Prentice hall, New Jersey, 1996.
[31] S.C. Reddy, D.S. Henningson, Energy growth in viscous channel flows, J. Fluid Mech. 252 (1993) 209238.
[32] S. Kandlikar, S. Garimella, D. Li, S. Colin, M.R. King, Heat Transfer and Fluid Flow in Minichannels and Microchannels, Elsevier, 2005.
[33] F.M. White, Fluid Mechanics, McGraw-Hill Education Ltd, 2011.